ACS APPLIED MATERIALS & INTERFACES

Research Article

www.acsami.org

Large Capacitance Enhancement Induced by Metal-Doping in Graphene-Based Supercapacitors: A First-Principles-Based Assessment

Eunsu Paek,[†] Alexander J. Pak,[†] and Gyeong S. Hwang*

Department of Chemical Engineering, University of Texas, Austin, Texas 78712, United States

Supporting Information

ABSTRACT: Chemically doped graphene-based materials have recently been explored as a means to improve the performance of supercapacitors. In this work, we investigate the effects of 3d transition metals bound to vacancy sites in graphene with [BMIM][PF_6] ionic liquid on the interfacial capacitance; these results are compared to the pristine graphene case with particular attention to the relative contributions of the quantum and electric double layer capacitances. Our study highlights that the presence of metal-vacancy complexes significantly increases the availability of electronic states near the charge neutrality point, thereby enhancing the quantum capacitance drastically. In addition, the use of metal-doped graphene electrodes is found to only marginally influence the microstructure and capacitance of the electric double layer. Our findings indicate that metal-doping of graphene-like electrodes can be a promising route toward increasing the interfacial capacitance of electrochemical double layer capacitors, primarily by enhancing the quantum capacitance.

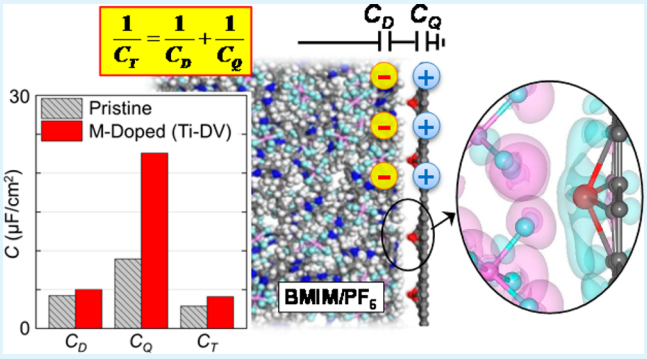

KEYWORDS: *quantum capacitance, electric double layer capacitance, ionic liquid, transition metal, density functional theory, molecular dynamics*

INTRODUCTION

Electrochemical double layer capacitors (EDLCs) are energy storage devices with high power densities and lifetimes.[1] Currently, graphene-based materials[2,3] and ionic liquids[4,5] (ILs) have garnered considerable interest as candidates for the electrode and electrolyte, respectively, in order to improve the capacitance and, thereby, the energy density. Modification of the electrode through doping or functionalization has been experimentally reported to further enhance the capacitance; this improvement is suggested to be broadly due to a combination of facilitated electrolyte wettability and electrode accessibility, increased electrical conductivity, and possible pseudocapacitance,[6−9] although the specific reasons are still unclear. According to very recent fundamental studies of the electrode−electrolyte interface, the total interfacial capacitance (C_T) of graphene-based EDLCs can be determined from both the electrode and electric double layer (EDL) capacitances (C_D) which are in series.[10−13] Furthermore, a series of theoretical work have demonstrated that the (electrode) quantum capacitance (C_Q), and thereby, C_T can be significantly enhanced as a result of changes in the electronic structure through dopants,[14] defects,[15] and/or structural deformation.[16,17]

Graphene-based materials decorated with metal (M) adatoms and/or nanoparticles have been widely studied as a means to induce doping;[18−23] the resulting modification of the electronic structure could significantly influence their performance for a variety of applications.[24−27] The electronic doping due to metal adsorbates has been thought to form a dipole layer at the metal/graphene interface, the so-called interfacial dipole layer.[19,20] More recently, several theoretical[28−30] and experimental[31,32] studies have shown that transition M atoms can be strongly bound to vacancy (V) defects along the graphene lattice. Using this approach, it may be possible to more precisely and dramatically alter the electronic structure of graphene, and subsequently the C_Q and C_D of the electrode−electrolyte interface, through controlled incorporation of desired dopant species and amounts. To date, however, the relative influence of M−V complexes on both C_Q and C_D, and therefore C_T, remains largely unexplored.

In this manuscript, we investigate the influence of metal incorporation in graphene on C_T based on a model system of M−V graphene complexes in [BMIM][PF_6] IL using a combined classical molecular dynamics (MD) and density functional theory (DFT) approach. In particular, we are interested in understanding the impact of M−V complexes

Received: March 8, 2014
Accepted: June 30, 2014
Published: July 1, 2014

on C_Q and C_D. Using DFT, we first study the electronic structure and C_Q of 3d M atoms bound to mono- and divacancy sites in graphene. We then employ MD simulations to study the microstructure and C_D at the electrode−electrolyte interface. Based on the relative contributions of C_Q and C_D to C_T, our work clearly demonstrates that the presence of M−V complexes can improve the overall performance of supercapacitors primarily by virtue of the enhanced C_Q.

RESULTS AND DISCUSSION

The Influence of Metal Dopants on the Electronic Structure and Quantum Capacitance. In this work, we investigate transition metals bound to two different graphene defect sites with a defect density (n_d) of 7.6×10^{13} cm^{-2}, as illustrated in Figure 1. To the left, a single metal (M) atom is

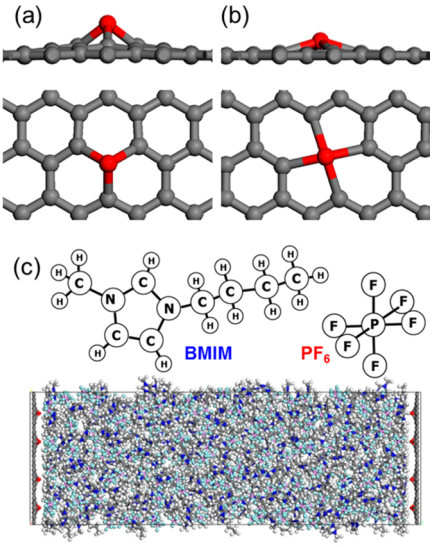

Figure 1. Top- and side-view schematics of a metal atom bound to the (a) monovacancy and (b) divacancy site, as well as schematics for (c) BMIM, PF_6, and the simulation box. White, blue, and gray balls indicate H, N, and C atoms in BMIM while pink and cyan balls indicate P and F atoms in PF_6. Red and gray balls represent the metal and C atoms of the electrode.

bound to a monovacancy (MV) site of graphene, which hereafter will be referred to as the M−MV complex; the M is bonded to the three nearest C atoms while also tending to lie out-of-plane. On the right, the M is bound to a divacancy (DV) site, which we call the M−DV complex; the M is now coordinated to the four nearest C atoms. While each of the M−C bond lengths for the M−DV complexes are larger than that of the M−MV complex, the M elevation is also smaller. In fact, Ni, Cu, and Zn tend to be planar with the graphene lattice. All binding energies and details of the geometry (bond length and M elevation) can be found in Figures S1 and S2, respectively. In addition, the calculated magnetic moments were found to be in good agreement with previous studies[29,30] and can be found in Figure S3.

The presence of M impurities and/or C vacancies can affect the electronic structure of graphene. But before analyzing the M−V complexes, we first examine the electronic density of states (DOS) of the unreconstructed MV defect; note that the unreconstructed MV defect has D_{3h} symmetry, unlike the fully relaxed MV defect which has C_{2v} symmetry.[33] As shown in Figure 2, near the Fermi level (E_F), we observe the existence of

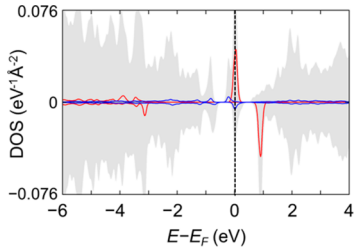

Figure 2. Total density of states (shaded) and the projected $2sp^2$ (red) and $2p_z$ (blue) orbitals of the undercoordinated C atoms at the monovacancy site. Positive (negative) values refer to the spin-majority (-minority) case. The Fermi level is indicated by the dashed line.

both sp^2 dangling bond and p_z states arising from the three undercoordinated C atoms; here, the p_z peak appears to be 1 eV below the sp^2 peak (which is doubly degenerate). Having identified these quasi-localized p_z and sp^2 states around the vacancy site, we now explore their hybridization with the M 3d states.

Figure 3 depicts a molecular orbital model[30] near E_F for the Ti case which serves as an example for the M−MV complexes;

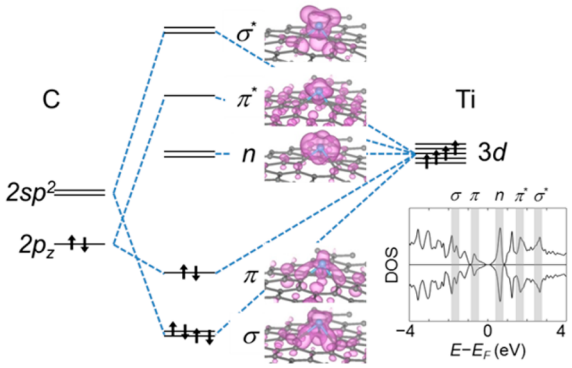

Figure 3. Schematic of the hybridization between the 3d orbitals of Ti and the $2sp^2$ and $2p_z$ orbitals of the C atoms at the monovacancy site, showing direct (σ), indirect (π), and non (n) bonding states. The depicted band-decomposed charge density isosurfaces (isosurface values of 0.005 e/bohr^3 for σ, n, σ^*, and 0.002 e/bohr^3 for π and π^*) were calculated from the shaded regions shown in the total density of states (DOS) (lower right).

note that the M−C interaction is dictated by the orbital overlap between C $2sp^2$ and $2p_z$ and M 3d states, while the emptied M 3s states are found well above E_F.[30] The overlap between the C sp^2 and out-of-plane M d_{xz} and d_{yz} orbitals can result in $\sigma-\sigma^*$ states as shown in the band-decomposed charge density isosurfaces; this is possible since the M atom is elevated with respect to the graphene lattice. In addition, $\pi-\pi^*$ states arise from the hybridization of C p_z and M d_z^2 orbitals, as also seen from the band-decomposed charge density isosurfaces; the π (π^*) state is expected to have a majority fraction of p_z (d_z^2) character. The in-plane d_{xy} and $d_{x^2-y^2}$ orbitals, which are elevated with respect to the graphene lattice, remain largely nonbonding.

Figure 4 shows the PDOS of the M d and the three neighboring C sp^2 and p_z orbitals for each M−MV complex (the total DOS is presented in Figure S4). We find that the predicted relative positions of the PDOS peaks are in good agreement with the model shown in Figure 3; as the number of valence d electrons increases from the Sc to Zn cases, the

dx.doi.org/10.1021/am501395j | ACS Appl. Mater. Interfaces 2014, 6, 12168−12176

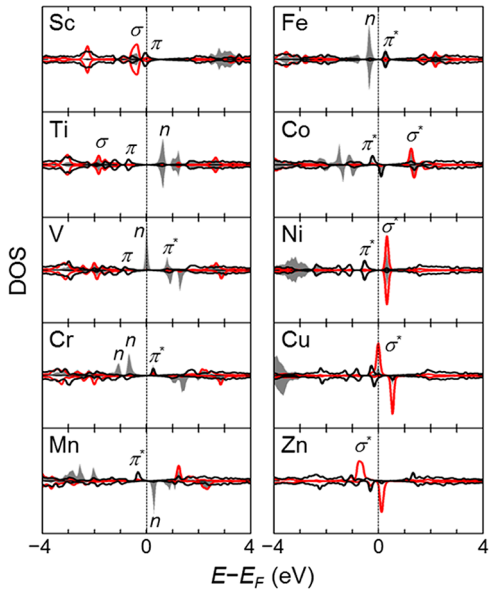

Figure 4. Spin-polarized density of states (DOS) projected onto the metal 3d orbitals (shaded) and $2sp^2$ (red) and $2p_z$ (black) orbitals of the C atoms at the monovacancy site; positive (negative) values refer to the spin-majority (-minority) state. The $2sp^2$ and $2p_z$ curves have been amplified by a factor of 2 and 5, respectively, for emphasis. The dashed line indicates the position of the Fermi level. The peaks near the Fermi level have been labeled to indicate the corresponding metal−carbon hybridization, as described in the text.

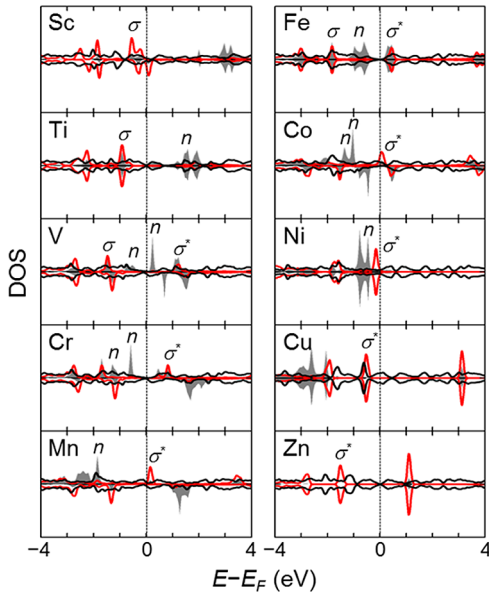

Figure 5. Spin-polarized density of states (DOS) projected onto the metal 3d orbitals (shaded) and $2sp^2$ (red) and $2p_z$ (black) orbitals of the C atoms at the divacancy site; positive (negative) values refer to the spin-majority (-minority) state. The $2sp^2$ and $2p_z$ curves have been amplified by a factor of 2 and 5, respectively, for emphasis. The dashed line indicates the position of the Fermi level. The peaks near the Fermi level have been labeled to indicate the corresponding metal−carbon hybridization, as described in the text.

previously identified M−C states are progressively filled. As an example, consider the Sc and Ti cases which have occupied σ and π states within $-1 < E - E_F < 0.5$ eV and $-2 < E - E_F < -0.5$ eV, respectively. In the former case, the π state is partially filled (with zero magnetic moment [Figure S3]), which suggests that Sc tends to accept an electron from the π system of graphene.[30] In addition when compared to the Sc case, the Ti case exhibits increased hybridization between the sp^2 and d_{xz} and d_{yz} orbitals, as suggested by the broadened features of the corresponding peak (indicated by σ) located around $-2 < E - E_F < -1.5$ eV; this is consistent with the fact that Ti has the larger binding energy [Figure S1]. The nonbonding states are occupied next as demonstrated by the V, Cr, Mn, and Fe cases; these states are indicated by the sharp d PDOS peaks, reflecting the localization of the d_{xy} and $d_{x^2-y^2}$ states, which tend to appear within $-1 < E - E_F < 1$ eV. Note that in the V, Cr, and Mn cases, the spin-majority nonbonding and π^* states are filled sequentially since a high-spin configuration is favored. Subsequently, the π^* and σ^* states are successively filled in the Co, Ni, Cu, and Zn cases, which is also well demonstrated by the decreased binding affinity of Cu and Zn compared to the other M atoms [Figure S1].

We next similarly analyzed the electronic structure of the M−DV complexes; the PDOS plots for the M−DV cases are depicted in Figure 5 (the total DOS is shown in Figure S4). Here, the bonding nature of the M to the DV site differs from that of the MV site in several distinct ways. First, the C sp^2 orbitals and in-plane M $d_{x^2-y^2}$ orbitals overlap to form $\sigma-\sigma^*$ states, as demonstrated by the band-decomposed charge density isosurfaces [Figure S5]; the $d_{x^2-y^2}$ orbitals tend to hybridize with the out-of-plane d_{xz} and d_{yz} orbitals [Figure S5]. Note that in the Sc case, the σ state is partially filled (with magnetic moment 0.4 μ_B [Figure S3]), which suggests that Sc accepts an electron from the π system of graphene (yet to a lesser extent than in the M−MV case). The second major difference is the absence of $\pi-\pi^*$ states (between C p_z and M d_z^2) due to the extended separation between M and C atoms [Figure S2]. As a result, the M d_z^2 and d_{xy} orbitals remain nonbonding [as seen in the band-decomposed charge density isosurfaces in Figure S5] and appear as sharp d PDOS peaks within $-1 < E - E_F < 1$ eV in the V through Ni cases. In addition, the PDOS of p_z tends to be broadened within the depicted window, suggesting that the p_z orbitals remain well-coupled to the extended π system. The final distinction is observed in the Cu and Zn cases in which the π^* states are filled; note that the binding energy of Cu and Zn in the DV case is predicted to be larger than that of the MV case [Figure S1].

From the band-decomposed charge density isosurfaces, we also observe that the aforementioned M−C hybrid states can be partially coupled to the extended π system of graphene. Therefore, we can expect the majority fraction of injected charge carriers to spread over the graphene lattice with some accumulation near the M atom. In addition upon binding to the vacancy site, we also expect charge to be transferred from the M atom to graphene, which we can quantify using Bader analysis[34] [Figure S6]. In the next section, we explore the impact of this charge redistribution on how these M−V complexes interact with [BMIM][PF_6] IL at the electrode−electrolyte interface. Here we should note that the quantitative predictions presented hitherto, particularly in the Mn case, may require further refinement since conventional DFT is well-known to underestimate the electron localization.[35] However, given the metallic nature of these M−C hybrid states, we can expect conventional DFT to adequately characterize the electronic structure.

From the DOS, the quantum capacitance (C_Q) is calculated from[12]

$$C_Q = e^2 \int_{-\infty}^{+\infty} D(E) F_T(E - \mu)\, dE$$

where e is the elementary charge, $D(E)$ is the electronic DOS, $F_T(E)$ is the thermal broadening function [$= (4k_BT)^{-1}\,\mathrm{sech}^2(E/2k_BT)$], and E is the energy with respect to the Fermi level E_F. Figure 6 shows the calculated C_Q of the M−MV [left] and M−DV [right] complexes at 300 K as a function of local potential (ϕ_G), which tend to resemble the respective DOS profiles under thermal broadening.

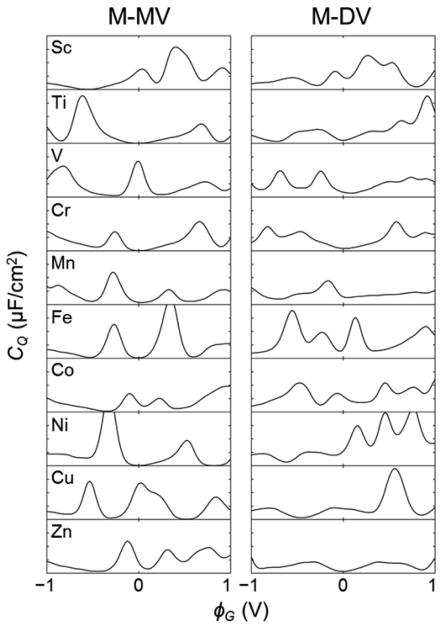

Figure 6. Predicted quantum capacitance (C_Q) values for electrodes with the listed metals bound to a monovacancy (M−MV) or divacancy (M−DV) site as a function of local electrode potential (ϕ_G). In each panel, C_Q ranges from 0 to 200 μF/cm^2.

In order to analyze the charging behavior of the electrode, we next compute the excess surface charge density (σ) as a function of ϕ_G in Figure 7 and compare it to that of pristine graphene; note that $\sigma = \int_0^{\phi_G} C_Q\, d\phi$. From Figure 7, it is abundantly clear that each of the M−MV and M−DV complexes store significantly more charge than pristine graphene [shaded] within a 2 V window. Note that in several M−MV cases (most notably in the Sc case but also in the V, Cr, and Mn cases), σ profile exhibits plateaus due to the lack of available electron states. In comparison, the monotonic increase in the σ profiles for the M−DV cases remains quite agnostic of metal dopant type. These plateau-like features are consistent with the fact that the impurity states tend to be more localized in the M−MV cases.

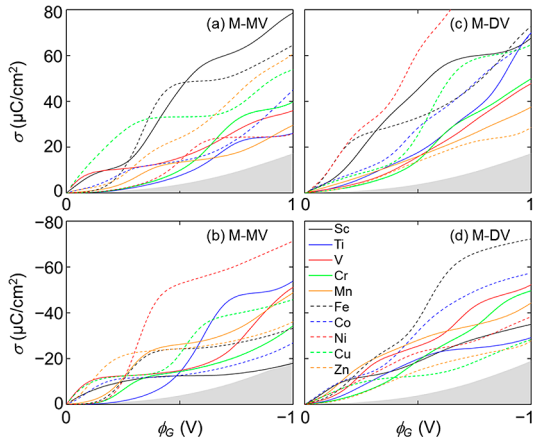

Figure 7. Excess electrode charge density (σ) as a function of local electrode potential (ϕ_G) for graphene with a metal atom bound to a monovacancy (M−MV) (a and b) and divacancy (M−DV) (c and d) site. The upper (lower) panels refer to the cathode (anode). The shaded region represents pristine graphene.

Impact of Metal Doping on the Electric Double Layer Microstructure and Capacitance. We next investigate the impact of the M−MV and M−DV graphene electrodes with $n_d = 7.6 \times 10^{13}$ cm^{-2} immersed in [BMIM][PF$_6$] IL on the electric double layer (EDL) microstructure and subsequently, the (integral) EDL capacitance (C_D). Specifically, we use MD simulations to examine how the doping-induced charge redistribution and the elevation of the M atom influence the EDL; note that the microstructure is influenced by only nonbonding interactions that are sufficiently captured using Coulomb and Lennard-Jones potentials, therefore precluding the use of more complex and computationally expensive reactive force fields such as ReaxFF.[36] We have chosen to study Ti−MV, Ti−DV, Ni−MV, and Ni−DV complexes in order to study a wide range of M atom elevations and partial charges; for example, the elevation of the M atom in Ni−MV and Ni−DV complexes varies by 1.35 Å (with similar partial charges) and the partial charge of the M atom in the Ti−DV and Ni−MV cases varies by around 1 e (with similar elevation). Table 1 summarizes the elevation and partial charge of the M atom used in the MD simulations for each M−V complex; note that a rectangular cell was used in these calculations.

Table 1. Summary of the Metal Atom Elevation and Partial Charge at Varying σ (μC/cm^2) Calculated from Density Functional Theory and Used in Classical Molecular Dynamics Simulations

	elevation	partial charge (σ = 0)	partial charge (σ = −4.7)	partial charge (σ = +4.7)
	Å	e	e	e
Ti−MV	1.8	1.37	1.33	1.39
Ti−DV	1.0	1.52	1.49	1.54
Ni−MV	1.35	0.50	0.47	0.53
Ni−DV	0.0	0.63	0.62	0.65

Near Uncharged Electrodes. In Figure 8a−d, we compare the mass density (ρ_m) profiles of BMIM and PF$_6$ near (a) Ti−MV, (b) Ti−DV, (c) Ni−MV, and (d) Ni−DV graphene electrodes as a function of distance from the electrode (z). All four cases exhibit oscillatory profiles that dampen away from the electrode, which is indicative of IL layering,[37−39] and

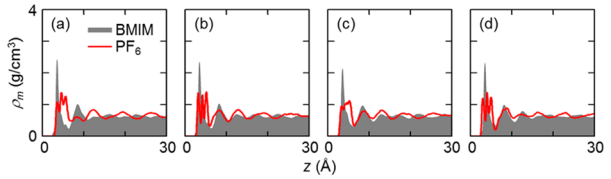

Figure 8. Mass density (ρ_m) profiles for BMIM and PF$_6$ as a function of distance from the electrode (z) for the (a) Ti−MV, (b)Ti−DV, (c) Ni−MV, and (d) Ni−DV cases when σ = 0 μC/cm^2.

dx.doi.org/10.1021/am501395j | ACS Appl. Mater. Interfaces 2014, 6, 12168−12176

become bulk-like after 3 nm. In every case, the first BMIM peak is quite pronounced, which demonstrates that the BMIM ring and tail retain the well-known parallel alignment with the graphene sheet, similarly to the pristine graphene case.[37−39] However, the three PF_6 peaks in the first layer ($z \approx 3-5$ Å) become noticeably less pronounced when the M atom elevation exceeds 1 Å, indicating that the PF_6 ions lose the well-known distinct orientation of parallel planes of F, P, and F atoms observed near planar electrodes.[12] For both PF_6 and BMIM, the preferential orientation of the first IL layer near pristine graphene is due to the electrode−electrolyte van der Waals (vdW) interactions. The charge redistribution due to the M−V complexes, however, introduces electrostatic interactions which can dominate over vdW interactions. As a result, PF_6 ions are electrostatically attracted toward the electropositive M atom; when the M atom is sufficiently elevated (>1 Å), PF_6 also rotates to more efficiently screen the M atom, thereby losing its previous orientation. BMIM ions, on the other hand, remain flat due to a combination of vdW and electrostatic attraction to the slightly electronegative graphene lattice. To clarify this behavior, we depict a snapshot of the Ti−MV electrode with adjacent IL ions in Figure S7.

In the case of pristine graphene, the number density of BMIM and PF_6 (and ρ_m given the similarity of their molecular weights) in each layer tends to be nearly equal in order to maintain charge neutrality.[12] This is also observed to be true in the Ni−DV case despite the large fluctuation of charge along the lattice (the partial charge of Ni is 0.63 e in this case) since Ni remains within the graphene plane. However, in the other three metal-doped cases, the spatial number density balance between BMIM and PF_6 is no longer maintained. For example, the second IL layer ($z \approx 9$ Å) exhibits an increasingly broadened PF_6 peak as the displacement of the M atom increases while the BMIM peak remains nearly the same. This suggests that due to the presence of the M atoms, ions segregate within the EDL to varying degrees. We can quantify this behavior using χ (the mixing parameter) as a function of z:

$$\chi_i(z) = \frac{\int_0^z \frac{\rho_{m,i}(z')}{MW_i}\,dz'}{\int_0^z \sum_j \frac{\rho_{m,j}(z')}{MW_j}\,dz'}$$

where i refers to the ion species of interest, j refers to each ion species present, and MW is the molecular weight. In this case when $\chi_i = 0.5$, the cumulative number of ion i is perfectly balanced by the other ion species. Figure 9 depicts χ_{BMIM} for each case studied; around $2 < z < 5$ Å, it is evident that χ_{BMIM} increases as the elevation of the M atom increases, which is consistent with the aforementioned competition (synergism) of electrostatic and vdW interactions between the electrode and PF_6 (BMIM).

From the distribution of electrode and IL atoms with fixed atomic charges, we can also compute the space charge variation (ρ_q, not shown). We then obtain the potential variation (ϕ) by solving Poisson's equation:

$$\nabla^2\phi = -\frac{\rho_q}{\varepsilon_0}$$

where ε_0 is the vacuum permittivity (details are described in the Supporting Information). In Figure 10, we show ϕ as a function of z for (a) Ti−MV, (b) Ti−DV, (c) Ni−MV, and (d) Ni−DV; the ϕ of the bulk electrolyte is taken as reference ($\phi = 0$ V). To

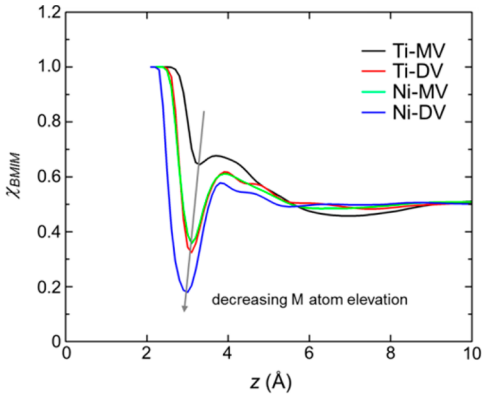

Figure 9. Mixing parameter (χ_{BMIM}) profiles for BMIM near uncharged electrodes as a function of distance from the electrode (z).

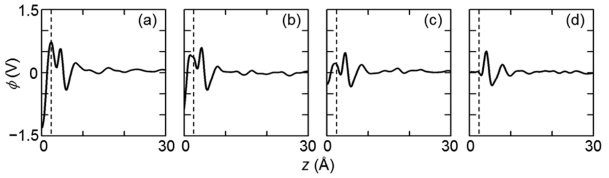

Figure 10. Potential (ϕ) profiles as a function of distance from the electrode (z) for the (a) Ti−MV, (b) Ti−DV, (c) Ni−MV, (d) Ni−DV cases when $\sigma = 0$ μC/cm^2. The dashed lines indicate the position of the vacuum−IL interface adjacent to the electrode.

interpret the ϕ profiles, it is helpful to separately examine their variation in the IL region and the near-electrode region between the electrode and first IL layer. First, we study how the microstructure of the IL ions affects ϕ close to the electrode ($2 < z < 5$ Å) as this is where discrepancies in the IL region between the different cases noticeably appear. In accordance with an increasing degree of BMIM segregation (Ni−DV < Ti−DV ≈ Ni−MV < Ti−MV cases), ϕ at the IL region interface ($z \approx 5$ Å) also increases; the accumulation of net positive charge close to the interface leads to a proportional increase in ϕ. Between the electrode and the IL region interface, however, ϕ rapidly drops if the M atom is elevated due to the local electric field generated from the charge redistribution within the electrode; the extent of the drop in ϕ therefore increases as either the M atom elevation and/or the charge differential between the M atom and graphene lattice increases. As a result of both of these factors, the surface potential relative to the bulk potential, otherwise known as the potential of zero charge (ϕ_Z), varies as 0.01 > −0.31 > −0.89 > −1.35 V for the Ni−DV > Ni−MV > Ti−DV > Ti−MV cases. We should note that in the pristine graphene case, ϕ_Z is predicted to be essentially zero.[12,40]

Near Charged Electrodes. Figure 11 shows the ρ_m profiles for BMIM and PF_6 for the Ti−MV, Ti−DV, Ni−MV, and Ni−DV cases, respectively when $\sigma = -4.75$ μC/cm^2 (a−d) and $\sigma = 4.75$ μC/cm^2 (e−h). Near each charged electrode, the ρ_m profiles exhibit alternating counterion/co-ion layering that dampens away from the electrode and extends around 3 nm before showing bulklike characteristics; this layering behavior is consistent with previous experimental studies near charged surfaces.[41−43] Near the negative electrode, the first BMIM peak tends to be very pronounced, indicating the well-known preference for the positively charged BMIM rings to align parallel to the electronegative graphene lattice due to electrostatic attraction.[12,38,39] At the same time, the presence

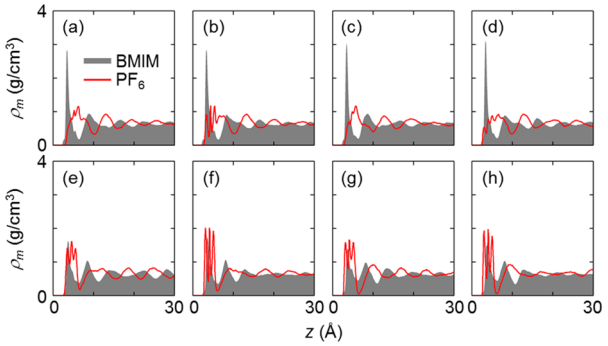

Figure 11. Mass density (ρ_m) profiles for BMIM and PF_6 as a function of distance from the electrode (z) for the (a) Ti−MV, (b) Ti−DV, (c) Ni−MV, and (d) Ni−DV cases when $\sigma = -4.75$ $\mu C/cm^2$ and for the (e) Ti−MV, (f) Ti−DV, (g) Ni−MV, (h) Ni−DV cases when $\sigma = 4.75$ $\mu C/cm^2$.

of PF_6 is shifted away from the electrode and loses its preferential orientation due to electrostatic repulsion; note that the PF_6 profile retains those initial three peaks in the Ti−DV case which suggests the preservation of some order. Near the positive electrode, the three PF_6 peaks in the first layer (representing F, P, and F atoms, respectively) are also pronounced. Yet similarly to when the electrodes are neutral, the rigidity of the PF_6 orientation is diminished when the M atom elevation exceeds 1 Å.

To further clarify the nature of the microstructure, we calculate χ for the counterion near each electrode, as shown in Figure 12a and b. Near the negative electrode, it is apparent

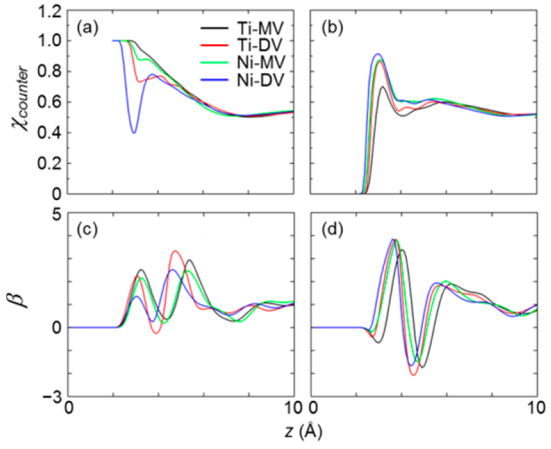

Figure 12. Mixing parameter ($\chi_{counter}$) profiles for the counterion and screening parameter (β) profiles as a function of distance from the electrode (z) when $\sigma = -4.75$ $\mu C/cm^2$ (a and c) and $\sigma = 4.75$ $\mu C/cm^2$ (b and d).

that the degree of BMIM segregation decreases directly with the M atom elevation. In contrast, the degree of PF_6 segregation increases inversely with the M atom elevation. Both of these observations are consistent with the previously described interaction of the M atom with PF_6 and BMIM, which is predominately electrostatic in nature.

By affecting the ion segregation near the electrode, the M−V complexes also alter the screening efficiency which can be quantified with β (the screening parameter) as a function of z:

$$\beta = -\frac{\int_0^z \rho_q(z')\,dz'}{\sigma}$$

where $\beta = 1$ indicates perfect screening of the electrode charge. Our results, shown in Figure 12c and d, show that the IL ions in the first layer overscreen the near-surface electric field, which is typical at small voltages.[44] Here, the impact of ion segregation on the IL screening becomes immediately obvious—the increased counterion segregation expectedly increases the overscreening as demonstrated by the comparative intensities of the first β peaks. Also note that the location of the β peaks shifts away from the electrode in accordance with the M atom elevation, further supporting the ion segregation behavior.

Figure 13 shows the predicted variation in ϕ near the negative (a−d) and positive (e−h) electrodes for each defect

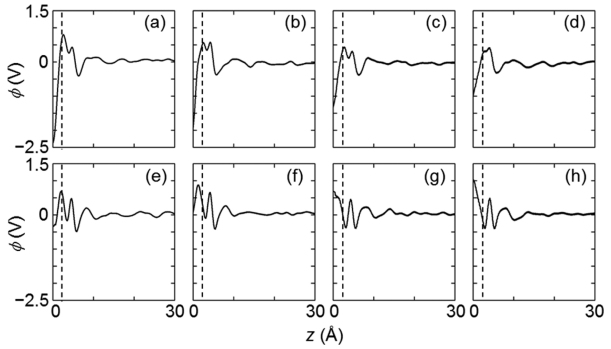

Figure 13. Potential (ϕ) profiles as a function of distance from the electrode (z) when $\sigma = -4.75$ $\mu C/cm^2$ for (a) Ti−MV, (b) Ti−DV, (c) Ni−MV, and (d) Ni−DV and when $\sigma = 4.75$ $\mu C/cm^2$ for (e) Ti−MV, (f) Ti−DV, (g) Ni−MV, and (h) Ni−DV. The dashed line indicates the position of the vacuum−IL interface adjacent to the electrode.

case. Near the negative (positive) electrode, the overall increase (decrease) in ϕ in the IL region ($2 < z < 5$ Å) becomes greater in proportion to the degree of counterion segregation (or by analogy, the extent of overscreening). From the IL region interface to the electrode surface, ϕ expectedly drops (rises) near the negative (positive) electrode due to the applied electric field. Here, ϕ is further influenced if the M atom is elevated due to the local electric field generated from the charge redistribution of the electrode. As the M atom elevation and/or partial charge increases, the drop (rise) in ϕ is enhanced (mitigated) near the negative (positive) electrode.

From the predicted electrode surface potentials relative to the bulk potential (ϕ_D), we calculate the overall change in potential as the difference between ϕ_D and ϕ_Z. We can therefore evaluate the (integral) double layer capacitances $C_D = \sigma/(\phi_D - \phi_Z)$, which we extend to include $\sigma = \pm 2.38$ and ± 9.5 $\mu C/cm^2$, and compare them in Figure 14. Although ϕ_Z widely varies, it is evident that the variation in C_D (and $\phi_D - \phi_Z$) is only as much as 20%; this suggests that the observed perturbations to the microstructure due to differences in M atom elevation and partial charge only weakly influence C_D. Furthermore, our results indicate that the presence of these M−V complexes consistently enhances C_D near the cathode (by as much as 20%) when compared to the pristine graphene case with $\sigma = 4.75$ $\mu C/cm^2$ (extrapolated from ref 12). However, near the anode, the C_D of the metal-doped cases tend to fluctuate around that of pristine graphene.

dx.doi.org/10.1021/am501395j | ACS Appl. Mater. Interfaces 2014, 6, 12168−12176

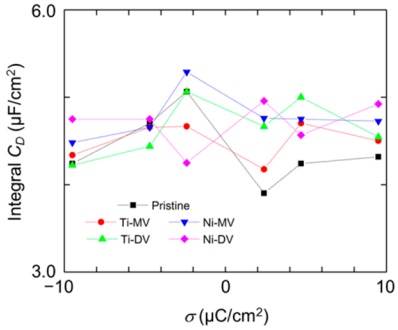

Figure 14. Integral double layer capacitance (C_D) as a function of excess surface charge density (σ) for Ti−MV, Ti−DV, Ni−MV, Ni−DV and pristine graphene cases. Results for pristine graphene were extrapolated from ref 12. The dashed lines are to guide the reader's eye.

Metal-Doping Effect on the Total Interfacial Capacitance. We estimate the total interfacial capacitance (C_T) as a function of applied potential ($\phi_a = \phi_G + \phi_D - \phi_Z$) when σ = ±2.38, ±4.75, and ±9.50 μC/cm^2 based on the series capacitance of C_D and C_Q, i.e. $1/C_T = 1/C_D + 1/C_Q$; note that the integral C_Q ($= \sigma/\phi_G$) is used here. As seen in Figure 15, the C_T of the metal-doped cases are predicted to

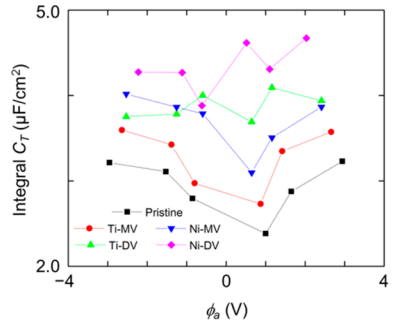

Figure 15. Predicted total interfacial capacitance (C_T) values for each metal-doped graphene case as a function of applied potential (ϕ_a). For reference, the C_T of pristine graphene in [BMIM][PF$_6$] IL is also included. The dashed line is to guide the reader's eye.

consistently outperform that of pristine graphene at both the anode and cathode; the Ni−DV case is particularly noteworthy with an enhancement of around 1−2 μF/cm^2 within ±1 V. We can attribute this improvement to the increased C_Q of the M−V complexes studied (the integral C_Q tend to vary significantly between 8 and 92 μF/cm^2) since the influence of metal-doping on C_D is marginal. These results suggest that metal-doping can be an effective strategy to mitigate the C_Q limitation of sp^2-bonded carbon electrodes, thereby allowing further improvements in C_D (whether through structural or other modifications) to manifest in the overall performance of supercapacitors.

We should point out that our quantitative prediction for C_T is based on several assumptions; the following factors should be considered in future investigations to improve accuracy. For instance, we have ignored the possible polarization at the electrode−electrolyte interface,[45] which can affect the electrode charge redistribution, the EDL microstructure, and ultimately, C_D (which is likely underestimated). In addition, we recognize that conventional DFT can introduce self-interaction errors; the resultant erroneous description of charge localization can be mitigated using hybrid functional methods.[46] We also omit the possible influence of IL interactions with the electrode on its electronic structure, which may alter C_Q to a certain extent. Nonetheless, our study clearly shows that the inclusion of M impurities in sp^2-bonded carbon nanomaterials can significantly enhance EDLC performance primarily by dramatically improving C_Q.

SUMMARY

We examined the influence of metal-doped graphene in [BMIM][PF$_6$] ionic liquid on the electrode and electric double layer (EDL) capacitances using a combination of DFT and classical MD simulations. We considered 3d transition metals (M) bound to mono- (MV) and di- (DV) vacancy sites in graphene. Our electronic structure analysis demonstrated that the introduction of these M−V complexes induces quasi-localized states. From the predicted electronic density of states, we evaluated the quantum capacitance (C_Q) of each M-doped electrode and compared them to pristine graphene. Due to the augmented availability of states, the charge storage capacities of each M-doped electrode were generally found to exceed that of pristine graphene, and in some cases, by as much as 500% (at a local potential of 1 V). We also studied the influence of these M−V complexes on the EDL microstructure using a few selected cases as model systems. We found that the microstructure can be perturbed; in particular, PF$_6$ (BMIM) ions can accumulate near (spread away from) the M atom. When the electrodes are charged, counterion segregation becomes more (less) apparent near the cathode (anode) as the M atom elevation increases. Despite these perturbations to the EDL, the estimated double layer capacitance (C_D) was found to be mostly within 20% of the pristine graphene case (while the potential of zero charge was predicted to vary on the order of 1 V depending on the type of M−V complex). Based on C_Q and C_D, we evaluated the total interfacial capacitances ($C_T = [1/C_D + 1/C_Q]^{-1}$) and found that the M-doped cases were consistently enhanced by as much as 125% (within ±1 V) when compared to pristine graphene. Our study clearly demonstrates that M-doping of graphene-like electrodes can effectively mitigate the C_Q limitation, thereby significantly enhancing EDLC performance.

COMPUTATIONAL METHODS

Density Functional Theory. The atomic and electronic structures of each M−V complex were calculated using DFT within the Perdew−Burke−Ernzerhof generalized gradient approximation[47] (GGA-PBE), as implemented in the Vienna Ab initio Simulation Package[48] (VASP). We employed the projector augmented wave (PAW) method[49] to describe the interaction between core and valence electrons, and a planewave basis set with a kinetic energy cutoff of E_{cut} = 400 eV. The pristine and M-doped graphene sheets were modeled using a 5 × 5 hexagonal supercell with the GGA-optimized lattice constant of 2.466 Å (which is slightly larger than the experimental value of 2.461 Å); each supercell had one metal atom and 49 (48) C atoms in the M−MV (M−DV) cases, corresponding to a defect density of 7.6 × 10^{13} cm^{-2}. Periodic boundary conditions were employed in all three directions with a vacuum gap of 10 Å in the vertical direction to separate the graphene system from its periodic images. For the Brillouin zone integration, we used a (12 × 12 × 1) Monkhorst−Pack[50] (MP) k-point mesh for geometry optimization and energy calculations, and a (15 × 15 × 1) MP k-point mesh to ensure convergence for electronic structure calculations. Details on the calculations for pristine graphene can be found in ref 12. Metal-doping induced charge redistributions were determined using grid-based Bader analysis.[34]

Classical Molecular Dynamics. We employed MD simulations with the OPLS-AA force field[51,52] to determine the microstructure of [BMIM][PF_6] and potential near the selected electrodes when σ = 0, ±2.38, ±4.75, and ±9.50 $\mu C/cm^2$. The Lennard-Jones parameters for Ti and Ni were adopted from previous work by Heinz and co-workers[53] and Minonishia and co-workers;[54] details on other force field parameters can be found in ref 12. As illustrated in Figure 1, the simulation domain consists of 356 [BMIM][PF_6] IL pairs sandwiched between two electrodes (34.18 Å × 39.46 Å) separated by 100 Å in the *z*-direction with periodic boundary conditions in the *x*- and *y*-directions. Here, the structure and charge distribution of the electrodes were determined from DFT calculations (additional details are summarized in Table 1). Note that we set the domain large enough such that the electrolyte maintains a bulk density of 1.33 g/cm^3, which is close to experimental values.[55] We annealed and quenched each MD simulation initially at 1000 K for 1 ns followed by 1 ns at 300 K for two cycles, and then further equilibrated for 3 ns at 300 K using a time step of 1 fs. Production runs were carried out for 4 ns with atomic positions recorded every 5 ps. All runs were in the NVT ensemble with the target temperature controlled by a Nose–Hoover thermostat[56] with a 100 fs damping parameter. All MD simulations were performed with the Large-scale Atomic/Molecular Massively Parallel Simulator (LAMMPS) program.[57] MD results reported herein were obtained from the average of five independent simulations with different initial atomic configurations.

■ ASSOCIATED CONTENT

Ⓢ Supporting Information

Additional content is available that includes the calculated binding energies, geometric data, magnetic moments, total DOS, and band-decomposed charge density isosurfaces, and Bader charge distributions concerning M–V complexes. A snapshot of the first IL layer in the Ti–MV case is also included. In addition, further details on the method used to solve Poisson's equation are provided. This material is available free of charge via the Internet at http://pubs.acs.org/.

■ AUTHOR INFORMATION

Corresponding Author

*E-mail: gshwang@che.utexas.edu.

Author Contributions

†E.P. and A.J.P. contributed equally to this work.

Notes

The authors declare no competing financial interest.

■ ACKNOWLEDGMENTS

This work was supported by the R.A. Welch Foundation (F-1535). We would also like to thank the Texas Advanced Computing Center for use of the Stampede supercomputing system (OCI-1134872).

■ REFERENCES

(1) Conway, B. E. *Electrochemical Supercapacitors: Scientific Fundamentals and Technological Applications*; Kluwar Academic: New York, 1999.

(2) Wang, G.; Zhang, L.; Zhang, J. A Review of Electrode Materials for Electrochemical Supercapacitors. *Chem. Soc. Rev.* **2012**, *41*, 797–828.

(3) Simon, P.; Gogotsi, Y. Capacitive Energy Storage in Nanostructured Carbon-Electrolyte Systems. *Acc. Chem. Res.* **2013**, *46*, 1094–1103.

(4) Armand, M.; Endres, F.; MacFarlane, D. R.; Ohno, H.; Scrosati, B. Ionic-liquid Materials for the Electrochemical Challenges of the Future. *Nat. Mater.* **2009**, *8*, 621–629.

(5) Liu, H.; Liu, Y.; Li, J. Ionic Liquids in Surface Electrochemistry. *Phys. Chem. Chem. Phys.* **2010**, *12*, 1685–1697.

(6) Qiu, Y.; Zhang, X.; Yang, S. High Performance Supercapacitors based on Highly Conductive Nitrogen-doped Graphene Sheets. *Phys. Chem. Chem. Phys.* **2011**, *13*, 12554–12558.

(7) Jeong, H. M.; Lee, J. W.; Shin, W. H.; Choi, Y. J.; Shin, H. J.; Kang, J. K.; Choi, J. W. Nitrogen-doped Graphene for High-Performance Ultracapacitors and the Importance of Nitrogen-doped Sites at Basal Planes. *Nano Lett.* **2011**, *11*, 2472–2477.

(8) Jiang, B.; Tian, C.; Wang, L.; Sun, L.; Chen, C.; Nong, X.; Qiao, Y.; Fu, H. Highly Concentrated, Stable Nitrogen-doped Graphene for Supercapacitors: Simultaneous Doping and Reduction. *Appl. Surf. Sci.* **2012**, *258*, 3438–3443.

(9) Sun, L.; Wang, L.; Tian, C.; Tan, T.; Xie, Y.; Shi, K.; Li, M.; Fu, H. Nitrogen-doped Graphene with High Nitrogen Level via a One-Step Hydrothermal Reaction of Graphene Oxide with Urea for Superior Capacitive Energy Storage. *RSC Adv.* **2012**, *2*, 4498–4506.

(10) Xia, J.; Chen, F.; Li, J.; Tao, N. Measurement of the Quantum Capacitance of Graphene. *Nat. Nanotechnol.* **2009**, *4*, 505–509.

(11) Stoller, M. D.; Magnuson, C. W.; Zhu, Y.; Murali, S.; Suk, J. W.; Piner, R.; Ruoff, R. S. Interfacial Capacitance of Single Layer Graphene. *Energy Environ. Sci.* **2011**, *4*, 4685–4689.

(12) Paek, E.; Pak, A. J.; Hwang, G. S. A Computational Study of the Interfacial Structure and Capacitance of Graphene in [BMIM][PF_6] Ionic Liquid. *J. Electrochem. Soc.* **2013**, *160*, A1–A10.

(13) Zhang, L. L.; Zhao, X.; Ji, H.; Stoller, M. D.; Lai, L.; Murali, S.; Mcdonnell, S.; Cleveger, B.; Wallace, R. M.; Ruoff, R. S. Nitrogen Doping of Graphene and Its Effect on Quantum Capacitance, and a New Insight on the Enhanced Capacitance of N-doped Carbon. *Energy Environ. Sci.* **2012**, *5*, 9618–9625.

(14) Paek, E.; Pak, A. J.; Kweon, K. E.; Hwang, G. S. On the Origin of the Enhanced Supercapacitor Performance of Nitrogen-doped Graphene. *J. Phys. Chem. C* **2013**, *117*, 5610–5616.

(15) Pak, A. J.; Paek, E.; Hwang, G. S. Tailoring the Performance of Graphene-based Supercapacitors using Topological Defects: A Theoretical Assessment. *Carbon* **2014**, *68*, 734–41.

(16) Pak, A. J.; Paek, E.; Hwang, G. S. Relative Contributions of Quantum and Double Layer Capacitance to the Supercapacitor Performance of Carbon Nanotubes in an Ionic Liquid. *Phys. Chem. Chem. Phys.* **2013**, *15*, 19741–19747.

(17) Paek, E.; Pak, A. J.; Hwang, G. S. Curvature Effects on the Interfacial Capacitance of Carbon Nanotubes in an Ionic Liquid. *J. Phys. Chem. C* **2013**, *117*, 23539–23546.

(18) Mao, Y.; Yuan, J.; Zhong, J. Density Functional Calculation of Transition Metal Adatom Adsorption on Graphene. *J. Phys.: Condens. Matter* **2008**, *20*, 115209.

(19) Giovannetti, G.; Khomyakov, P.; Brocks, G.; Karpan, V.; van den Brink, J.; Kelly, P. Doping Graphene with Metal Contacts. *Phys. Rev. Lett.* **2008**, *101*, 026803.

(20) Pi, K.; McCreary, K.; Bao, W.; Han, W.; Chiang, Y.; Li, Y.; Tsai, S.-W.; Lau, C.; Kawakami, R. Electronic Doping and Scattering by Transition Metals on Graphene. *Phys. Rev. B* **2009**, *80*, 075406.

(21) Cao, C.; Wu, M.; Jiang, J.; Cheng, H.-P. Transition Metal Adatom and Dimer Adsorbed on Graphene: Induced Magnetization and Electronic Structures. *Phys. Rev. B* **2010**, *81*, 205424.

(22) Gupta, S. K.; Soni, H. R.; Jha, P. K. Electronic and Phonon Bandstructures of Pristine Few Layer and Metal Doped Graphene Using First Principles Calculations. *AIP Adv.* **2013**, *3*, 032117.

(23) Santos, J. E.; Peres, N. M. R.; Lopes dos Santos, J. M. B.; Castro Neto, A. H. Electronic Doping of Graphene by Deposited Transition Metal Atoms. *Phys. Rev. B* **2011**, *84*, 085430.

(24) Gutés, A.; Hsia, B.; Sussman, A.; Mickelson, W.; Zettl, A.; Carraro, C.; Maboudian, R. Graphene Decoration with Metal Nanoparticles: Towards Easy Integration for Sensing Applications. *Nanoscale* **2012**, *4*, 438–440.

(25) Vadahanambi, S.; Jung, J.-H.; Oh, I.-K. Microwave Syntheses of Graphene and Graphene Decorated with Metal Nanoparticles. *Carbon N. Y.* **2011**, *49*, 4449–4457.

(26) Ren, Y.; Chen, S.; Cai, W.; Zhu, Y.; Zhu, C.; Ruoff, R. S. Controlling the Electrical Transport Properties of Graphene by in Situ Metal Deposition. *Appl. Phys. Lett.* **2010**, *97*, 053107.

(27) Giovanni, M.; Poh, H. L.; Ambrosi, A.; Zhao, G.; Sofer, Z.; Šaněk, F.; Khezri, B.; Webster, R. D.; Pumera, M. Noble Metal (Pd, Ru, Rh, Pt, Au, Ag) Doped Graphene Hybrids for Electrocatalysis. *Nanoscale* **2012**, *4*, 5002−5008.
(28) Kim, G.; Jhi, S.-H.; Lim, S.; Park, N. Effect of Vacancy Defects in Graphene on Metal Anchoring and Hydrogen Adsorption. *Appl. Phys. Lett.* **2009**, *94*, 173102.
(29) Krasheninnikov, A. V.; Lehtinen, P. O.; Foster, A. S.; Pyykkö, P.; Nieminen, R. M. Embedding Transition-Metal Atoms in Graphene: Structure, Bonding, and Magnetism. *Phys. Rev. Lett.* **2009**, *102*, 126807.
(30) Santos, E. J. G.; Ayuela, A.; Sánchez-Portal, D. First-Principles Study of Substitutional Metal Impurities in Graphene: Structural, Electronic and Magnetic Properties. *New J. Phys.* **2010**, *12*, 053012.
(31) Rodríguez-Manzo, J. A.; Cretu, O.; Banhart, F. Trapping of Metal Atoms in Vacancies of Carbon Nanotubes and Graphene. *ACS Nano* **2010**, *4*, 3422−3428.
(32) Wang, H.; Wang, Q.; Cheng, Y.; Li, K.; Yao, Y.; Zhang, Q.; Dong, C.; Wang, P.; Schwingenschlögl, U.; Yang, W.; Zhang, Z. Z. Doping Monolayer Graphene with Single Atom Substitutions. *Nano Lett.* **2012**, *12*, 141−144.
(33) El-Barbary, A. A.; Telling, R. H.; Ewels, C. P.; Heggie, M. I.; Briddon, P. R. Structure and Energetics of the Vacancy in Graphite. *Phys. Rev. B* **2003**, *68*, 144107.
(34) Henkelman, G.; Arnaldsson, A.; Jónsson, H. A Fast and Robust Algorithm for Bader Decomposition of Charge Density. *Comput. Mater. Sci.* **2006**, *36*, 354−360.
(35) Wu, M.; Cao, C.; Jiang, J. Z. Electronic Structure of Substitutionally Mn-doped Graphene. *New J. Phys.* **2010**, *12*, 063020.
(36) van Duin, A. C. T.; Dasgupta, S.; Lorant, F.; Goddard, W. A. ReaxFF: A Reactive Force Field for Hydrocarbons. *J. Phys. Chem. A* **2001**, *105*, 9396−9409.
(37) Maolin, S.; Fuchun, Z.; Guozhong, W.; Haiping, F.; Chunlei, W.; Shimou, C.; Yi, Z.; Jun, H. Ordering Layers of [bmim][PF_6] Ionic Liquid on Graphite Surfaces: Molecular Dynamics Simulation. *J. Chem. Phys.* **2008**, *128*, 134504.
(38) Kislenko, S. A.; Samoylov, I. S.; Amirov, R. H. Molecular Dynamics Simulation of the Electrochemical Interface Between a Graphite Surface and the Ionic Liquid [BMIM][PF_6]. *Phys. Chem. Chem. Phys.* **2009**, *11*, 5584−5590.
(39) Feng, G.; Qiao, R.; Huang, J.; Dai, S.; Sumpter, B. G.; Meunier, V. The Importance of Ion Size and Electrode Curvature on Electrical Double Layers in Ionic Liquids. *Phys. Chem. Chem. Phys.* **2011**, *13*, 1152−1161.
(40) Wang, S.; Li, S.; Cao, Z.; Yan, T. Molecular Dynamic Simulations of Ionic Liquids at Graphite Surface. *J. Phys. Chem. C* **2010**, *114*, 990−995.
(41) Mezger, M.; Schröder, H.; Reichert, H.; Schramm, S.; Okasinski, J. S.; Schöder, S.; Honkimäki, V.; Deutsch, M.; Ocko, B. M.; Ralston, J.; Rohwerder, M.; Stratmann, M.; Dosch, H. Molecular Layering of Fluorinated Ionic Liquids at a Charged Sapphire (0001). *Surf. Sci.* **2008**, *322*, 424−428.
(42) Liu, Y.; Zhang, Y.; Wu, G.; Hu, J. Coexistence of Liquid and Solid Phases of Bmim-PF6 Ionic Liquid on Mica Surfaces at Room Temperature. *J. Am. Chem. Soc.* **2006**, *128*, 7456−7457.
(43) Bovio, S.; Podesta, A.; Lenardi, C.; Milani, P.; Na, C. I. M. I.; Fisica, D. Evidence of Extended Solidlike Layering in [Bmim][NTf2] Ionic Liquid Thin Films At Room-Temperature. *J. Phys. Chem. B* **2009**, 6600−6603.
(44) Bazant, M. Z.; Storey, B. D.; Kornyshev, A. A. Double Layer in Ionic Liquids: Overscreening Vs. Crowding. *Phys. Rev. Lett.* **2011**, *106*, 046102.
(45) Merlet, C.; Péan, C.; Rotenberg, B.; Madden, P. A.; Simon, P.; Salanne, M. Simulating Supercapacitors: Can We Model Electrodes As Constant Charge Surfaces? *J. Phys. Chem. Lett.* **2013**, *4*, 264−268.
(46) Cohen, A. J.; Mori-Sánchez, P.; Yang, W. Insights into Current Limitations of Density Functional Theory. *Science* **2008**, *321*, 792−794.
(47) Perdew, J. P.; Burke, K.; Ernzerhof, M. Generalized Gradient Approximation Made Simple. *Phys. Rev. Lett.* **1996**, *77*, 3865−3868.
(48) Kresse, G.; Furthmüller, J. Efficient Iterative Schemes for *Ab Initio* Total-Energy Calculations Using a Plane-Wave Basis Set. *J. Phys. Rev. B* **1996**, *54*, 11169−11186.
(49) Blöchl, P. E. Projector Augmented-Wave Method. *Phys. Rev. B* **1994**, *50*, 17953−17979.
(50) Monkhorst, H. J.; Pack, J. D. Special Points for Brillouin-Zone Integrations. *Phys. Rev. B* **1976**, *13*, 5188−92.
(51) Jorgensen, W. L.; Maxwell, D. S.; Tirado-Rives, J. Development and Testing of the OPLS All-Atom Force Field on Conformational Energetics and Properties of Organic Liquids. *J. Am. Chem. Soc.* **1996**, *118*, 11225−11236.
(52) Kaminski, G.; Jorgensen, W. L. Performance of the AMBER94, MMFF94, and OPLS-AA Force Fields for Modeling Organic Liquids. *J. Phys. Chem.* **1996**, *100*, 18010−18013.
(53) Heinz, H.; Vaia, R. A.; Farmer, B. L.; Naik, R. R. Accurate Simulation of Surfaces and Interfaces of Face-Centered Cubic Metals Using 12−6 and 9−6 Lennard-Jones Potentials. *J. Phys. Chem. C* **2008**, *112*, 17281−90.
(54) Minonishi, Y.; Ishioka, S.; Koiwa, M.; Morozumi, S.; Yamaguchi, M. The Core Structures of 1/3 < 1123> {1122} Edge Dislocations in H.C.P. Metals. *Philos. Mag. A* **1981**, *43*, 1017−26.
(55) Kumełan, J.; Kamps, Á. P.-S.; Tuma, D.; Maurer, G. Solubility of CO in the Ionic Liquid [bmim][PF_6]. *Fluid Phase Equilib.* **2005**, *228*−*229*, 207−211.
(56) Hoover, W. Canonical Dynamics: Equilibrium Phase-Space Distributions. *Phys. Rev. A* **1985**, *31*, 1695−1697.
(57) Plimpton, S. J. Fast Parallel Algorithms for Short-Range Molecular Dynamic. *J. Comput. Phys.* **1995**, *117*, 1−19.